Gate-Tunable Field-Compatible Fluxonium

Pita-Vidal, Marta; Bargerbos, Arno; Yang, Chung-Kai; van Woerkom, David J.; Pfaff, Wolfgang; Haider, Nadia; Krogstrup, Peter; Kouwenhoven, Leo P.; de Lange, Gijs; Kou, Angela

Gate-Tunable Field-Compatible Fluxonium

Marta Pita-Vidal [●],[1,2,*] Arno Bargerbos,[1,2] Chung-Kai Yang,[3] David J. van Woerkom,[3]
Wolfgang Pfaff [●],[4] Nadia Haider [●],[1,5] Peter Krogstrup,[6] Leo P. Kouwenhoven,[1,3] Gijs de Lange,[3] and
Angela Kou[4]

[1] *QuTech, Delft University of Technology, Delft 2628 CJ, Netherlands*
[2] *Kavli Institute for Nanoscience, Delft University of Technology, Delft 2628 CJ, Netherlands*
[3] *Microsoft Quantum Lab Delft, Delft 2628 CJ, Netherlands*
[4] *Department of Physics and Frederick Seitz Materials Research Laboratory, University of Illinois
Urbana-Champaign, Urbana, IL 61801, USA*
[5] *Netherlands Organisation for Applied Scientific Research (TNO), Delft 2628 CK, Netherlands*
[6] *Center for Quantum Devices, Niels Bohr Institute, University of Copenhagen, Copenhagen 2100, Denmark
Denmark and Microsoft Quantum Materials Lab Copenhagen, Lyngby 2800, Denmark*

Hybrid superconducting circuits, which integrate nonsuperconducting elements into a circuit quantum electrodynamics (cQED) architecture, expand the possible applications of cQED. Building hybrid circuits that work in large magnetic fields presents even further possibilities, such as the probing of spin-polarized Andreev bound states and the investigation of topological superconductivity. Here we present a magnetic-field compatible hybrid fluxonium with an electrostatically tuned semiconducting nanowire as its nonlinear element. We operate the fluxonium in magnetic fields up to 1 T and use it to observe the φ_0-Josephson effect. This combination of gate tunability and field compatibility opens avenues for the control of spin-polarized phenomena using superconducting circuits and enables the use of the fluxonium as a readout device for topological qubits.

I. INTRODUCTION

Circuit quantum electrodynamics (cQED), where photons are coherently coupled to artificial atoms built with superconducting circuits, has enabled the investigation and control of macroscopic quantum-mechanical phenomena in superconductors [1–3]. Recently, hybrid circuits incorporating semiconducting nanowires [4–7] and other electrostatically gateable elements [8–11] into superconducting circuits have broadened the scope of cQED to probing mesoscopic superconductivity [4,5,7, 12]. Further extending the capabilities of hybrid circuits to work in magnetic fields presents the intriguing possibility of insights into *topological* superconductivity [13–20].

Topological superconductivity, which has garnered much theoretical and experimental interest lately [21–24],

*m.pitavidal@tudelft.nl

results from the interplay between magnetism and superconductivity. In superconductor-proximitized semiconductors exposed to a large magnetic field, emergent quasiparticle states known as Majorana zero modes (MZMs) can form. Majorana zero modes are predicted to be robust to local perturbations and could thus serve as long-lived qubits. Several groups have proposed using superconducting circuits to both probe and control MZMs [14,17,18,20,25]. All of the above-mentioned proposals, however, require the operation of a flux-based superconducting circuit in large magnetic fields.

Additionally, the behavior of superconductor-proximitized semiconductors exposed to a large magnetic field in the trivial phase remains an active field of research. Most experiments investigating the behavior of Andreev bound states (ABSs) in a magnetic field have been focused on the magnetic-field dependence of the switching current [26–28] with the exceptions of Refs. [29] and [30], in which ABS spectroscopy was performed up to fields of 300 and 11 mT, respectively. Energies below 20 μeV, which are interesting for high-transparency ABSs and MZMs, were, however, not accessible. A fluxonium that works in high magnetic fields and with semiconducting weak

links would thus be an extremely useful tool both for investigating the magnetic field behavior of ABSs and also for coupling to topological superconductors. First, the fluxonium ground-to-excited state transitions are typically accessible at microwave frequencies over the entire flux range from 0 to π. One therefore gains access to the full energy-phase relations of the junction. Second, the Josephson energy of the junction can be known extremely precisely (to less than 0.4 μeV) and over multiple decades, which allows for the mapping of the characteristic energy of the semiconducting weak link. Finally, the fluxonium is also sensitive to quasiparticle poisoning events in individual ABSs in the junction since poisoning of individual ABSs would lead to additional spectral lines. Knowledge of these rates would greatly aid the design of Andreev-based qubits [12,31].

Moreover, the unique parameter regime of the fluxonium makes it particularly suited to detecting and controlling MZMs. A switch in the parity of MZMs coupled to the fluxonium circuit corresponds to a switch in the direction of the persistent current flowing in the fluxonium circuit. Parity switches of the MZMs would thus result in the observation of two copies of the fluxonium spectrum [25]. In addition, the presence of MZMs coupled to the fluxonium changes the periodicity of its spectrum from 2π to 4π. In these proposals, the linewidth of the fluxonium transition determines the sensitivity with which the fluxonium could determine the presence of MZMs. Beyond its detection capabilities, multiple fluxonium devices coupled to MZMs could also implement braiding operations on the MZMs [20].

Here we have realized a hybrid fluxonium incorporating an Al-proximitized nanowire that operates up to 1 T. We build upon recent work proximitizing semiconducting nanowires to incorporate a magnetic-field compatible, electrostatically tunable weak-link junction into the fluxonium [32]. The presented fluxonium device also has a gradiometric design and is composed of (Nb,Ti)N for further field compatibility. We demonstrate *in-situ* gate tunability of the fluxonium Josephson energy over more than a decade. We then operate the fluxonium in fields up to 1 T and map out the dependence of the fluxonium Josephson energy as a function of the field. In all regimes of magnetic field and gate voltage, we observe excellent agreement between the data and a theoretical model based on a simple Hamiltonian with a few degrees of freedom. Finally, we also demonstrate the utility of the fluxonium as a probe of mesoscopic superconductivity in magnetic fields by using the measured energy-phase relation of the junction to observe the φ_0-Josephson effect. The ability to observe the fluxonium spectrum over a wide range of gate voltages and magnetic fields establishes the hybrid fluxonium as a superconducting circuit for exploring superconducting phenomena in a magnetic field and as a realistic readout platform for MZMs.

II. MAGNETIC-FIELD-COMPATIBLE MATERIALS AND DESIGN

Building a fluxonium compatible with the application of a magnetic field presents multiple challenges. The first challenge is reaching the fluxonium regime using magnetic-field-compatible materials. The fluxonium consists of a Josephson junction with Josephson energy E_J in parallel with a linear superinductor [33], with inductive energy E_L, and a capacitor characterized by the energy E_C, as shown in Fig. 1(a). The fluxonium regime ($E_L < E_C < E_J$) is achieved by shunting the junction with a large inductance. This parameter regime results in the eigenstates of the fluxonium being composed of superpositions of persistent currents in multiple directions [Fig. 1(b)]. Additionally, the chosen fluxonium parameters result in a spectrum that is observable over the entire range of applied external flux. Superconductor-insulator-superconductor (*S-I-S*) Josephson junction arrays, commonly used to implement the fluxonium superinductance [33–35], cannot be used since they are incompatible with large magnetic fields. Recent work on magnetic-field-compatible materials with a large kinetic inductance, such as granular aluminium [36–39] and (Nb,Ti)N [40–42], has presented a path to meeting the stringent requirements of the fluxonium superinductance. The magnetic-field-compatible fluxonium device is shown in Figs. 1(c)–1(f). All circuit elements except for the junction are fabricated using (Nb,Ti)N, which has been demonstrated to have critical fields exceeding 9 T and inductances exceeding 75 pH/$\square$ [41]. Here we define the fluxonium by etching a 9-nm-thick sputtered (Nb,Ti)N film, which has a kinetic inductance of 41 pH/$\square$. The superinductance of the fluxonium is made with a 50-nm-wide (Nb,Ti)N meander [Fig. 1(e)] in order to maximize the inductance of the device while minimizing spurious capacitances to ground. This design realizes an inductance of approximately 100 nH. The small width of the meanders additionally suppresses the emergence of lossy vortices due to out-of-plane fields, B_x, up to tens of millitesla [43]. We further mitigate the effects of these vortices by introducing vortex-pinning holes [inset, Fig. 1(c)] into the capacitor of the fluxonium readout resonator and the ground plane.

In addition to being composed of magnetic-field-compatible materials, for use as a detector, the fluxonium must also maintain its narrow linewidth during the application of a magnetic field. The application of a magnetic field precludes the possibility of using the magnetic shielding necessary for limiting flux noise in flux-based superconducting circuits. We address this challenge by building a gradiometric superinductance as shown in Fig. 1(d). Equal fluxes through each of the two loops generate equal currents that are canceled at the junction, rendering the fluxonium insensitive to flux noise due to sources larger than the fluxonium device.
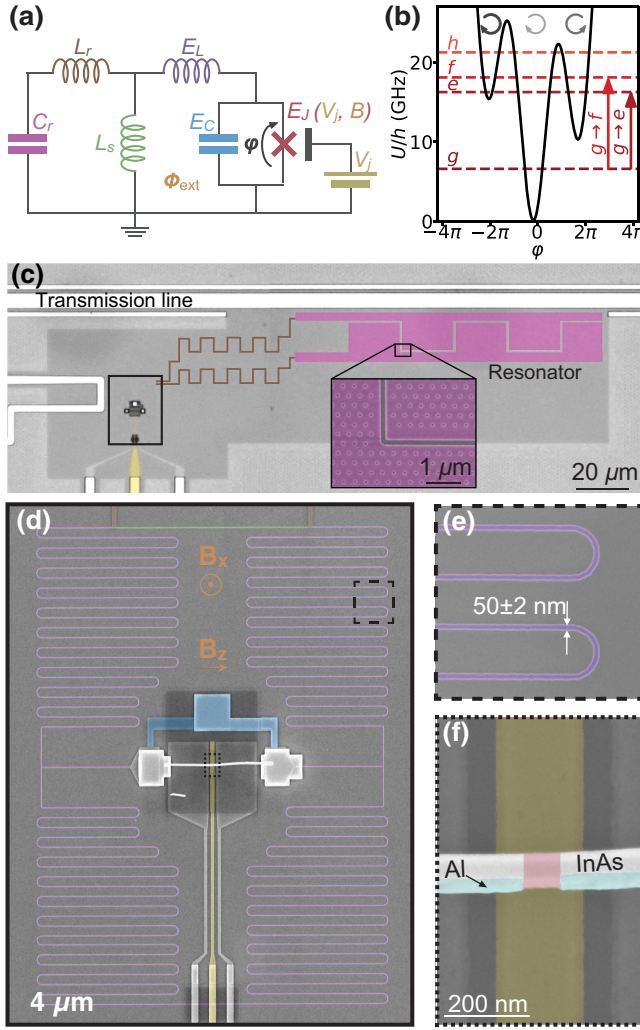
FIG. 1. Nanowire fluxonium. (a) Circuit model. The fluxonium is composed of a Josephson junction shunted by an inductor and a capacitor, which are characterized by the energies E_J, E_L, and E_C, respectively. The value of E_J depends on the external magnetic field B_z and the gate voltage V_j. A readout resonator (constituted by L_r and C_r) is coupled to the fluxonium via a shared inductance L_s. (b) Potential of the fluxonium (black) versus the phase difference across the junction, φ, at $\varphi_{ext} = 0.2\pi$. The lowest eigenenergies are indicated with dashed horizontal lines. Red arrows indicate transitions starting from the ground state. Circular gray arrows represent the amplitude and direction of the persistent-current states associated with different potential wells. (c) False-colored optical image showing the transmission line and the resonator, with capacitive and inductive elements shaded in pink and brown, respectively. Inset: Scanning electron microscope (SEM) image of the resonator's capacitive plates. (d) SEM image of a lithographically similar fluxonium to device A, corresponding to the area indicated by the box in (c). The (Nb,Ti)N superinductor [purple, enlarged in (e)], the shared inductance section (green), the parallel plate capacitor (blue), and the nanowire junction [red, enlarged in (f)] respectively correspond to the E_L, L_s, E_C, and E_J elements in (a). The out-of-plane component of B, B_x, tunes the external magnetic flux Φ_{ext}. Here B_z is the component parallel to the wire.

Finally, a *S-I-S* Josephson junction made of Al and AlO_x, which has been used in all previously reported fluxonium devices, cannot be used as the E_J element here due to its incompatibility with the magnetic field. We build a magnetic-field-compatible junction by incorporating a semiconducting InAs nanowire proximitized by an epitaxially grown 6-nm-thick aluminum layer [Fig. 1(f)] [32] into the fluxonium. The small thickness of the aluminum shell makes it resilient to magnetic fields along the wire of more than 1 T [32]. Similar resilience to magnetic fields could also be attained using weak links of disordered superconducting materials, such as indium oxide [44] or granular aluminum [45], as the Josephson junction. The nanowire is deterministically deposited on top of the prepatterned leads of the inductor and capacitor using a micromanipulator. The Josephson junction is then defined by etching away an Al section of approximately 80 nm on top of the junction gate. This small junction, however, does not provide a large enough capacitance to achieve the fluxonium regime for typical E_J values in nanowire junctions. We thus add a parallel plate capacitor [blue in Fig. 1(d)] to decrease E_C and achieve its required value for the fluxonium. The fluxonium capacitor consists of two square (Nb,Ti)N plates sandwiching a 29-nm-thick SiN dielectric. We note that this fluxonium design is flexible enough to incorporate any semiconducting material as its small junction.

III. FLUXONIUM SPECTROSCOPY

We first demonstrate that our device behaves as expected for a fluxonium coupled to a readout resonator. Data from two similar fluxonium devices (device A and device B) will be presented in this article. We first focus on the behavior of device A. We monitored the transmission amplitude, $|S_{21}|$, at frequencies $f_{r,drive}$ around the resonator frequency $f_{g0 \to g1}$, as a function of the external phase $\varphi_{ext} = (2e/\hbar)\Phi_{ext}$, as shown in the top panel of Fig. 2(a). Transitions are labeled as $m_i n_i \to m_e n_e$, where m_i (m_e) and n_i (n_e) are the initial (end) states of the fluxonium and resonator, respectively. The resonator spectrum is periodic in flux and also exhibits gaps in its visibility, which indicate that the resonator is coupled to the fluxonium. The bottom panel in Fig. 2(a) shows the flux dependence of the observed transition frequencies of the fluxonium-resonator system, measured by monitoring the transmission amplitude at $f_{r,drive} = f_{g0 \to g1}$ while the system is driven with a second tone with frequency $f_{f,drive}$, also via the resonator. Though the gradiometric loops that comprise the fluxonium are designed to be symmetric, the placement of the capacitor and gate lines inside them, together with inevitable imprecision when manually depositing the nanowire, lead to a small imbalance between the effective area of the two gradiometer loops. The imbalance allows us to thread a flux using an out-of-plane magnetic field,
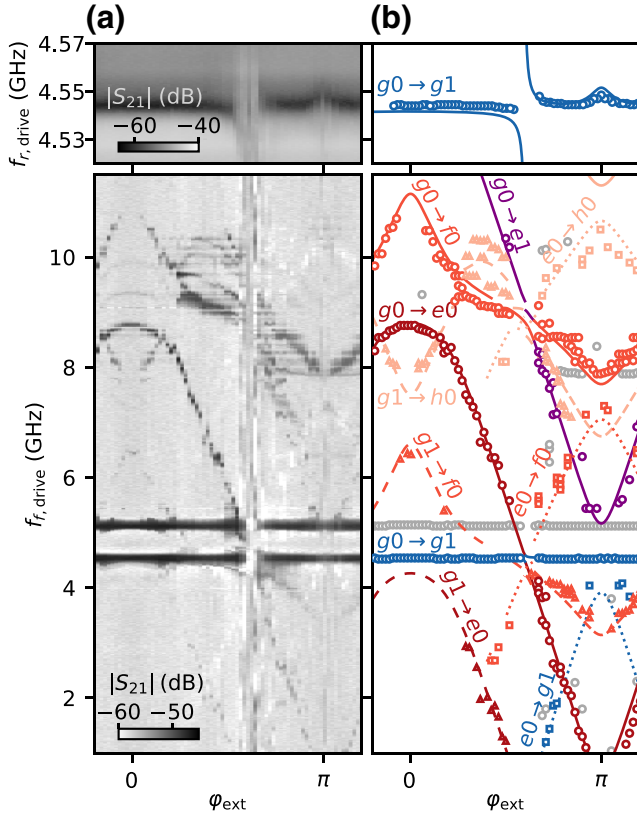
FIG. 2. Two-tone spectroscopy of device A, at $B_z = 0$. (a) Magnitude of the transmitted readout signal as a function of the external flux and $f_{r,\text{drive}}$ (top) and $f_{f,\text{drive}}$ (bottom), showing the flux modulation of the different transitions. (b) Extrema (maxima and minima) extracted from (a) (markers) and fitted transition frequencies (lines) obtained from the numerical diagonalization of the model Hamiltonian [Eq. (1)]. Gray markers indicate extrema that are not associated with any fluxonium-resonator transitions. A value of $E_J/h = 6.7$ GHz is extracted from the fit.

B_x. Threading a flux quantum through the gradiometer corresponds to $B_x = 550$ μT, which is much greater than the 15 μT that would be needed to thread a flux quantum through one of the two symmetric loops. The gradiometric geometry thus reduces the sensitivity of the fluxonium to magnetic field noise larger than the fluxonium loop by more than an order of magnitude.

To fit the spectroscopy data [markers in Fig. 2(b)], we diagonalize the Hamiltonian for the coupled fluxonium-resonator system shown in Fig. 1(a), $\hat{H}$ [46]. In the limit $L_f \gg L_s, L_r$ (where $L_f = \Phi_0^2/4\pi^2 E_L$ and $\Phi_0 = h/2e$),

$$\hat{H} = \frac{2e^2}{C_r}\hat{n}_r^2 + \frac{1}{2}\frac{(\Phi_0/2\pi)^2}{(L_r + L_s)}\hat{\varphi}_r^2 - \frac{1}{2}\frac{(\Phi_0/2\pi)^2 L_s}{L_f(L_r + L_s)}\hat{\varphi}_r\hat{\varphi}_f + \hat{H}_f,$$

$$\tag{1}$$

TABLE I. Device parameters obtained by fitting spectra in Figs. 2–4 and by electromagnetic simulations. Here h is Planck's constant.

	Device A	Device B
E_C/h (GHz)	2.35	1.75
E_L/h (GHz)	0.7	1.1
C_r (fF)	26	26
L_r (nH)	47	42
L_s (nH)	8.5	4.6

where

$$\hat{H}_f = 4E_C\hat{n}_f^2 - E_J(V_j, B)\cos(\hat{\varphi}_f) + \frac{1}{2}E_L(\hat{\varphi}_f - \varphi_{\text{ext}})^2 \tag{2}$$

is the Hamiltonian of the uncoupled fluxonium. Here, $\hat{\varphi}_f$ and $\hat{\varphi}_r$ are the phase drops across the fluxonium junction and across C_r, respectively, and $\hat{n}_f$ and $\hat{n}_r$ are their conjugated charges. We leave all circuit parameters free except for $C_r = 26$ fF, which we extract from electromagnetic simulations. The parameters obtained from the fit are shown in Table I and the fitted transition frequencies are denoted with lines in Fig. 2(b). Each state is identified by the closest state in energy for the uncoupled system. In addition to transitions originating from the ground state, $g0$, we also observe transitions for which the initial state is $g1$, with one photon in the resonator (dashed lines). This is due to the continuous drive used to monitor $|S_{21}|$ at $f_{g0\to g1}$, which can populate the resonator. Transitions starting from the first excited fluxonium state, $e0$, around $\varphi_{\text{ext}} = \pi$ (dotted lines) are also observed. The transition frequency for $g0 \to e0$ goes below 1 GHz near $\varphi_{\text{ext}} = \pi$. The transitions from $e0$ thus occur due to the expected equilibrium thermal occupation of $e0$ for temperatures of around 20 mK. We find excellent agreement between the experimental data and the fit, with all fit parameters coming to within 5% of the designed circuit parameters except for E_J, which we can only coarsely predict. We have etched a 80 nm junction to maximize E_J, but the specific values of E_J are determined by the interaction with the electrostatic gate and the microscopic details of the junction.

IV. ELECTROSTATIC TUNING OF FLUXONIUM PARAMETERS

Mesoscopic phenomena often require fine tuning of the charge carrier density in the semiconductor. We here demonstrate that the spectrum of the fluxonium is measurable over a large range of gate voltages and thus does not limit the possible observable phenomena. We first measure $f_{g0\to g1}$ vs V_j. As shown in Fig. 3(a), the resonator frequency is constant at low and high voltage values but has nonmonotonic fluctuations in an intermediate range, which is consistent with observations in previous experiments on nanowire junctions [4–6,29], where these fluctuations were
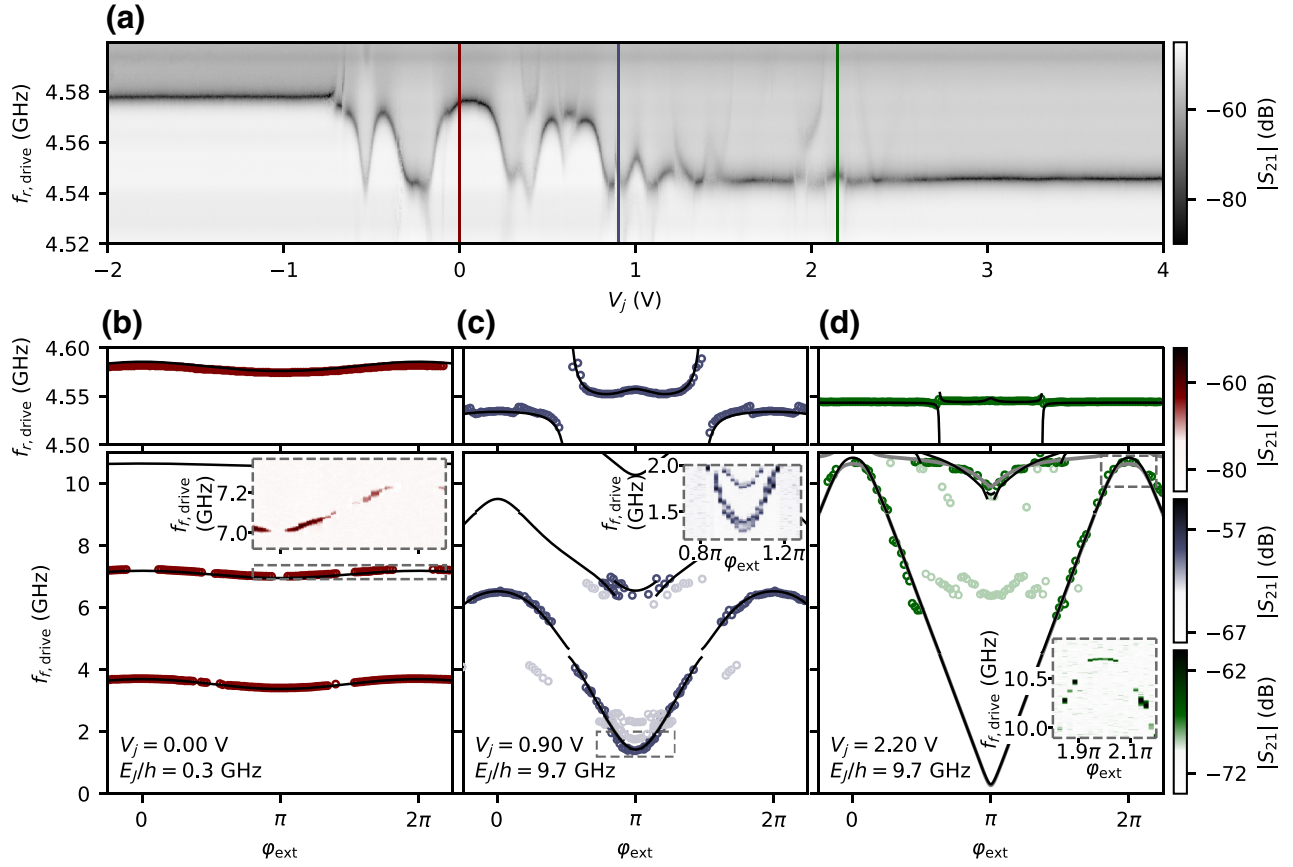
FIG. 3.   Gate tuning of E_J in device A, at $B_z = 0$. (a) Gate dependence of the resonator's resonant frequency, $f_{g0 \to g1}$, at $\varphi_{ext} = 1.25\pi$. (b)–(d) Fluxonium spectra at three different gate points, indicated with vertical lines in (a). The markers correspond to the peaks extracted from the measured resonator (top) and two-tone (bottom) transmission data. The fitted transition frequencies $f_{g0 \to e0}$, $f_{g0 \to f0}$, and $f_{g0 \to h0}$ (black lines) are obtained by fitting the darker markers with Hamiltonian (1). The values of E_J/h extracted are 0.2, 3.8, and 9.6 GHz, respectively. For (d), the spectrum can be fitted more accurately with a Hamiltonian including one highly transparent channel (gray lines). The insets in (b)–(d) show sections of the measured transmission magnitude. In (b) we observe gaps in visibility at zero and half flux in the $g0 \to f0$ transition.

attributed to consecutive openings of different junction channels in the nanowire, whose transparencies oscillate with the gate. The behavior of the $f_{g0 \to g1}$ transition provides insight into the V_j dependence of the fluxonium E_J. The value of $f_{g0 \to g1}$ can be seen as the bare resonant frequency of the uncoupled resonator plus a dispersive shift caused by the coupling to the fluxonium. The dispersive shift depends on the frequency of all level transitions of the coupled fluxonium-resonator system and is thus different for different values of E_J. This change in the dispersive shift leads to the observed changes in the measured resonant frequency of the resonator.

We now investigate directly the fluxonium spectrum. In Figs. 3(b)–3(d) we present spectra taken at three different V_j values [marked by solid lines in Fig. 3(a)]. Here we use a lower drive power than in Fig. 2 to reduce broadening of the spectral lines due to the drive power; therefore, the main observable transitions start from the ground state,

$g0$. For low V_j, we observe a weakly anharmonic spectrum [Fig. 3(b)]. For large V_j values [Figs. 3(c) and 3(d)], however, the flux dependence and the anharmonicity become much stronger. We also note the presence of additional transitions in the spectroscopy data for intermediate and large V_j denoted by the lighter markers in Figs. 3(c) and 3(d). The spectrum at intermediate V_j are taken at a point where the junction is very sensitive to the gate voltage; the additional transitions are due to the E_J of the junction fluctuating while the spectroscopy is being performed. At higher V_j, the E_J of the junction is stable as a function of the gate but additional transitions due to the presence of the resonator drive are also observed. We fit the data of the three spectra using the same parameters as those used in Fig. 2 while only allowing E_J to vary. The fits maintain their accuracy over the whole V_j range. We do note, however, that, for large E_J, the fit starts to deviate from the data for transitions to higher excited states [Fig. 3(d)]. This may

be due to a nonsinusoidal energy-phase relation of a more transparent channel in the junction. A fit using a Hamiltonian including the Andreev potential for a short transparent junction instead of the standard $\cos\varphi$ potential is shown in gray in Fig. 3(d). Details of the fit as well as additional fits to the data in Figs. 3(b) and 3(c) using the Andreev potential in the Hamiltonian can be found in the Appendix.

We have therefore shown that the behavior of a hybrid fluxonium circuit with a semiconducting weak link can still be predicted and understood using a simple Hamiltonian with a few degrees of freedom. Moreover, we can conclude that E_J is the only circuit parameter affected by large changes in V_j and that it generally increases with V_j. Our results thus show that it is possible to address and observe the state of the system over a large E_J range encompassing regimes where its eigenstates are of very different character.

V. FLUXONIUM BEHAVIOR IN A MAGNETIC FIELD

Next, we explore the magnetic field compatibility of the nanowire fluxonium. The magnetic field behavior of the device strongly depends on the microscopic details of the nanowire junction. In order to demonstrate the field compatibility of the fluxonium circuit elements, we here show data from device B whose parameters are optimized for magnetic field compatibility. The magnetic field behavior of device A is provided in the Supplemental Material [47]. Spectroscopy measurements at two different V_j and B_z points are shown in Figs. 4(a) and 4(b). We continue to be able to perform spectroscopy on the fluxonium over the full range in φ_{ext} at fields up to 1 T. We do note, however, that at higher magnetic fields, the thermal occupation of the excited state of the fluxonium does increase since we observe transitions from this state even when the $g0 \rightarrow e0$
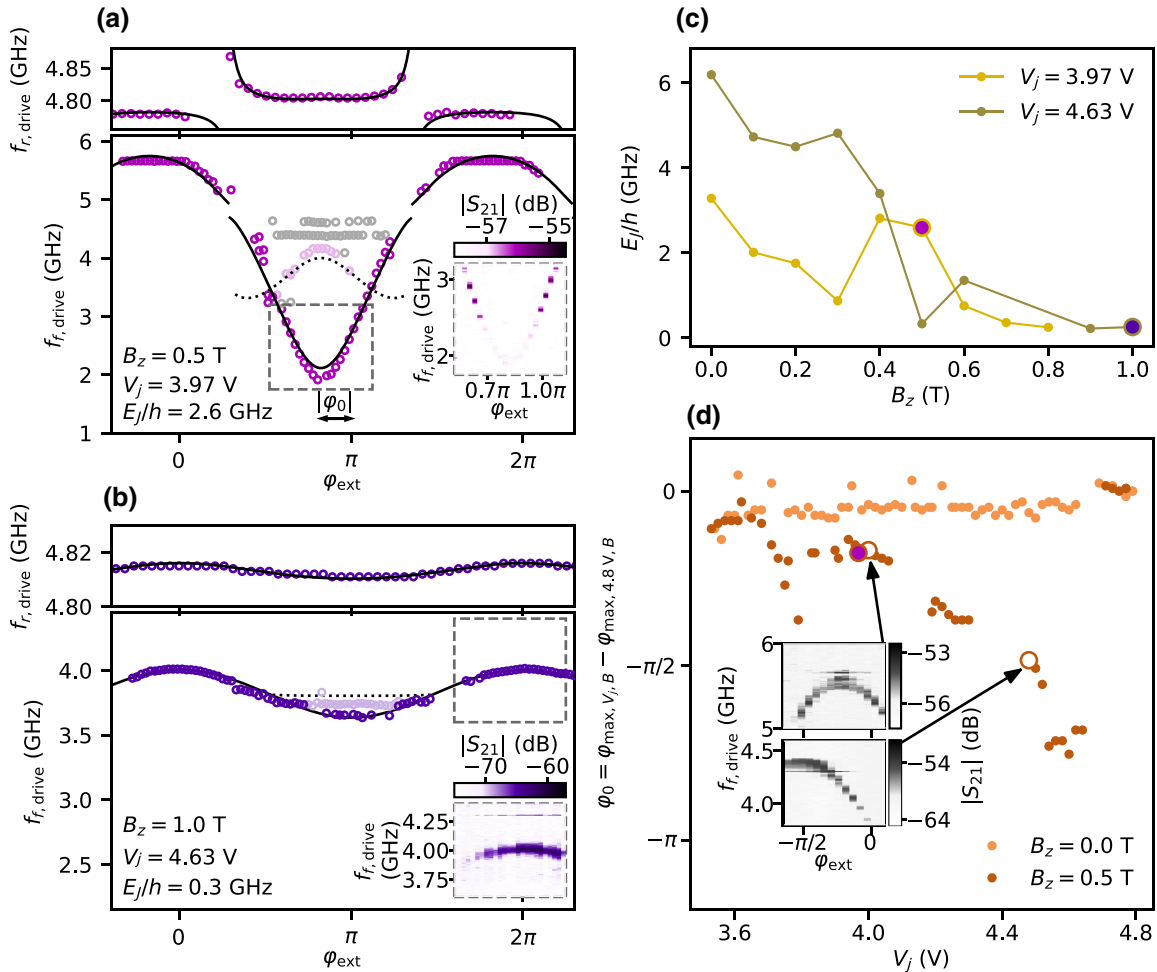

FIG. 4.   Behavior of device B in a magnetic field. (a),(b) Fluxonium spectra at two different V_j and B_z points. The E_J value extracted from the fit is lower at higher magnetic fields. In (a) we observe a $\varphi_0 = -0.16\pi$ phase shift with respect to a reference φ_{ext} taken at the same field at $V_j = 4.80$ V. (c) Plot of E_J vs B_z at two different gate voltage points. The E_J value decreases nonmonotonically with the field. (d) Plot of φ_0 vs V_j at two different magnetic field points. At $B_z = 0.0$ T, φ_0 stays constant for the whole V_j range. At $B_z = 0.5$ T, however, there is a continuous φ_0 shift that ranges from 0 to $-\pi$. The two insets show the zero-flux spectroscopy feature shifted from zero at two different gate points. In (c),(d) the points corresponding to the spectra in (a),(b) are highlighted with matching colors.

frequency is above 1 GHz. Importantly, we can still fit the spectroscopy data accurately in this regime, indicating that the fluxonium-resonator Hamiltonian remains valid at high magnetic fields, with E_J being the only parameter largely affected by B_z. Fit parameters for device B are shown in Table I.

We finally use the nanowire fluxonium to investigate the behavior of spin-orbit-coupled semiconducting junctions in a magnetic field. We perform spectroscopy measurements at gate voltages ranging from 3.5 to 4.8 V and fields ranging from 0 to 1 T. From the spectroscopy we extract E_J as a function of B_z at two different gate points, which is shown in Fig. 4(c). A nonmonotonic decrease of E_J with the field is observed at both gate points. We expect an overall decrease in E_J vs B_z due to the superconducting gap closing at high magnetic fields. The nonmonotonic behavior of E_J, however, suggests the presence of interference between different modes in the junction [27]. Additional in-field E_J data is provided in Sec. V of the Supplemental Material [47]. An overall decrease of E_J with B_z is observed for all investigated gate values, while the nonmonotonic dependence is often, but not always, observed.

A shifting of the zero-flux point in the spectroscopy of the fluxonium device at high fields can be used to determine the breaking of multiple symmetries in the semiconducting junction [48]. This phase shift is known as the φ_0-Josephson effect, which occurs when chiral and time-reversal symmetries are both broken in the junction. In InSb- and InAs-based junctions, this symmetry breaking originates from the interplay between the presence of multiple channels in the junction, spin-orbit coupling, and the Zeeman splitting due to the applied magnetic field [29,48,49]. We observe such a shift in the zero-flux point of the spectroscopy lines as V_j is varied in a B_z field [indicated by $\varphi_0 = \varphi_{\max,V_j,B} - \varphi_{\max,4.8V,B}$ in Fig. 4(a)]. The φ_0 shift as a function of V_j is shown, at $B_z = 0$ and at $B_z = 0.5$ T, in Fig. 4(d). The φ_0 value at $V_j = 4.80$ V is taken as the $\varphi_0 = 0$ reference at each B_z. The value of φ_0 is thus a relative value at each B_z. At $B_z = 0$ the zero-flux point does not change, while it changes continuously with V_j when a B_z field is applied. Since the observed phase shift appears as a function of only V_j at fixed magnetic fields, we can exclude trivial effects such as misalignment of the magnetic field. We note that we observe shifts in φ_0 approaching π, which is significantly larger than previously predicted [48]. Mixing between a large number of spin-split Andreev channels in the junction may lead to the larger observed shifts. Additional φ_0 data as a function of V_j and B can be found in the Supplemental Material [47].

VI. SPECTROSCOPIC LINEWIDTH

For the fluxonium's applications as a detector of field-dependent mesoscopic effects, its spectral lines must

be measurable under the magnetic field and electrostatic conditions of interest, but also must maintain a narrow linewidth in all regimes. The spectroscopic linewidth bounds the resolution with which we can resolve the splitting of lines due to, for example, quasiparticle poisoning of highly transparent ABSs or MZMs at the junction.

We have performed a spectroscopic linewidth analysis for devices A and B at different points in external flux (Fig. 5): near the flux sweet spot at $\varphi_{\text{ext}} = 0$ and also at $\varphi_{\text{ext}} = 0.3\pi$. As shown in Fig. 5(a), the linewidth of device B stays below 50 MHz up to 1 T at the $\varphi_{\text{ext}} = 0$. However, the linewidth overall becomes larger, for both
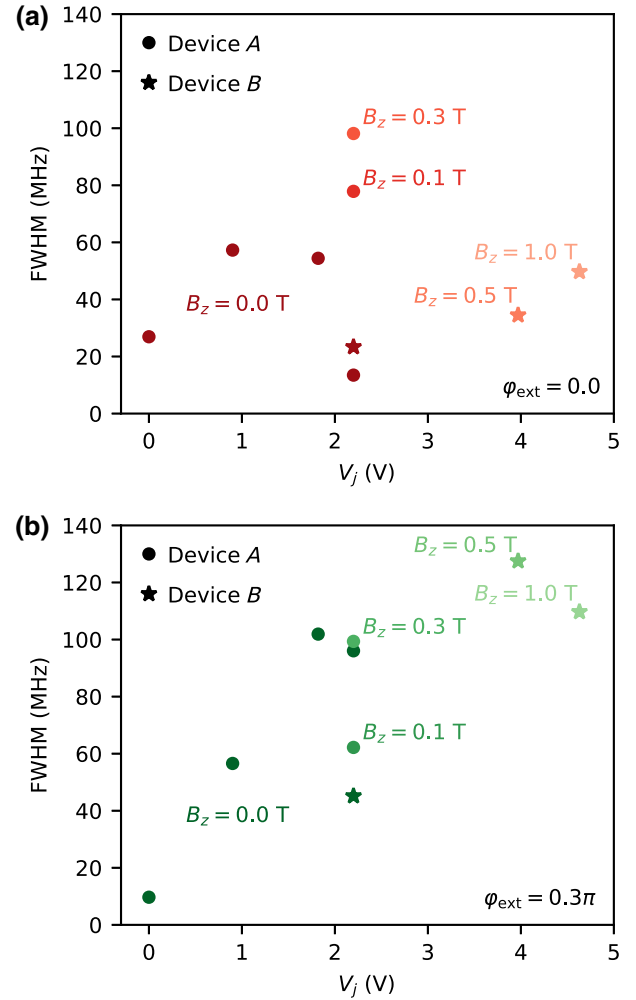

FIG. 5. Spectroscopic linewidth. Extracted linewidth [full width at half maximum (FWHM)] of the $g \to e$ transition as a function of V_j for device A (circular markers) and device B (star markers). Different color strengths denote different magnetic fields. The data for device A correspond to the spectra shown in Figs. 3(b)–3(d) and Fig. 2 of the Supplemental Material [47]. The in-field data for device B correspond to the spectra shown in Figs. 4(a) and 4(b). The linewidths are extracted in symmetric 0.05π flux windows around $\varphi_{\text{ext}} = 0$, which is a sweet spot for the external flux, and $\varphi_{\text{ext}} = 0.3\pi$ for (a),(b), respectively.

devices, at $\varphi_{\text{ext}} = 0.3\pi$ [Fig. 5(b)]. This behavior is consistent with residual flux noise broadening the linewidth of the fluxonium. Our linewidth analysis indicates that the energy resolution of the fluxonium would, if measuring near $\varphi_{\text{ext}} = 0$, be at most 0.4 μeV in all regimes, which significantly improves upon the resolution that can currently be reached by transport experiments where the linewidth is limited by thermal broadening (typically approximately 10 μeV).

We do note that in our experiment the fluxonium and resonator parameters are chosen for the greatest visibility over the largest range of E_J and φ_{ext}. Improvements upon the design, such as weaker coupling to the readout resonator, smaller asymmetry in the gradiometric superinductance, and materials optimizations such as changing the dielectric of the fluxonium capacitor, would lead to significantly narrower linewidths.

VII. CONCLUSION

In conclusion, we have successfully realized a gate-tunable fluxonium resilient to high magnetic fields. We have combined a gate-controlled junction with magnetic-field-compatible materials and a gradiometric design to build the hybrid fluxonium. We are able to perform spectroscopy over a large range of gate voltages and in-plane magnetic fields. We have used the fluxonium to investigate the behavior of an InAs Josephson junction in a magnetic field and observed a nonmonotonic decrease of the E_J of the junction as well as the φ_0-Josephson effect. The observed φ_0 shift is gate tunable up to $\varphi_0 = \pi$. One could therefore use this effect to build extremely small, flux-noise insensitive superconducting circuits where the phase difference of the junction could be tuned using a gate voltage.

The magnetic-field-compatible hybrid fluxonium is also now ready to detect the 4π-periodic Josephson effect [25] and measure Majorana parity dynamics. We remark that, while our experiment was performed with similar materials and in similar magnetic fields to previous experiments where transport signatures pointed to the presence of MZMs, we did not observe any signatures of MZMs. Recent theoretical work has suggested that previously observed signatures of MZMs may be due to trivial Andreev bound states [50] and has advocated for cleaner materials with stronger spin-orbit coupling proximitized by superconductors with larger energy gaps. Future experiments will thus incorporate InSb nanowires with thinner Al shells as the small junction of the hybrid fluxonium.

The excellent agreement we have demonstrated between data and theory indicates that one can engineer hybrid circuits such that their behavior can continue to be understood even when the circuit is complicated by the interplay of superconductivity, spin-orbit coupling, and magnetism.

This opens avenues for using the hybrid fluxonium to explore superconductivity in the presence of a magnetic field as well as reading out and controlling material platforms that require the application of a large magnetic field. Since it is straightforward to incorporate different materials into the hybrid fluxonium, proposals to probe superconductor-proximitized edge states in a quantum spin Hall insulator [51,52] or field-dependent spin-polarized correlated insulating phases [53,54] are now possible using our hybrid circuit.

APPENDIX: MODELING THE JUNCTION ACCOUNTING FOR HIGHLY TRANSPARENT TRANSMISSION CHANNELS

In Figs. 2–4 we fit the spectroscopy data assuming a sinusoidal current-phase relation at the junction, which results in the term $-E_J\cos(\varphi)$ in the Hamiltonian [Eq. (2)], which is characteristic of S-I-S junctions with low-transparency channels. A more accurate model for the potential of a semiconducting Josephson junction with N channels with transparencies T_i is [55]

$$V_{\text{SJJ}}(\varphi) = \Delta \sum_{i=1}^{N} \sqrt{1 - T_i\sin^2(\varphi/2)}, \qquad \text{(A1)}$$

where Δ denotes the induced gap on the proximitized sections of the nanowire. When the transparencies of the different channels are low, this dependence converges to a sinusoidal relation with $E_J = \Delta \sum_{i=1}^{N} T_i/4$.

Here, we show fits to the spectroscopy data from Fig. 3 using the semiconducting junction potential V_{SJJ} with a different number of channels and for various values of Δ. In Fig. 6 we show fits to the transitions starting from the ground state with the Hamiltonian for the uncoupled fluxonium [Eq. (2)] using a sinusoidal potential, a one-channel potential, and a two-channel potential. In Fig. 7 we show the Δ sensitivity of the one-channel spectrum, showing the fit accuracy for Δ values lower and higher than the optimum value. For low and intermediate E_J values, the accuracy of the different models is very similar. For high E_J, however, the fits to the high-frequency transitions are more accurate when highly transparent channels are included. This points toward the presence of at least one highly transparent channel in the junction. The fit accuracy is however similar when one, two, or more channels
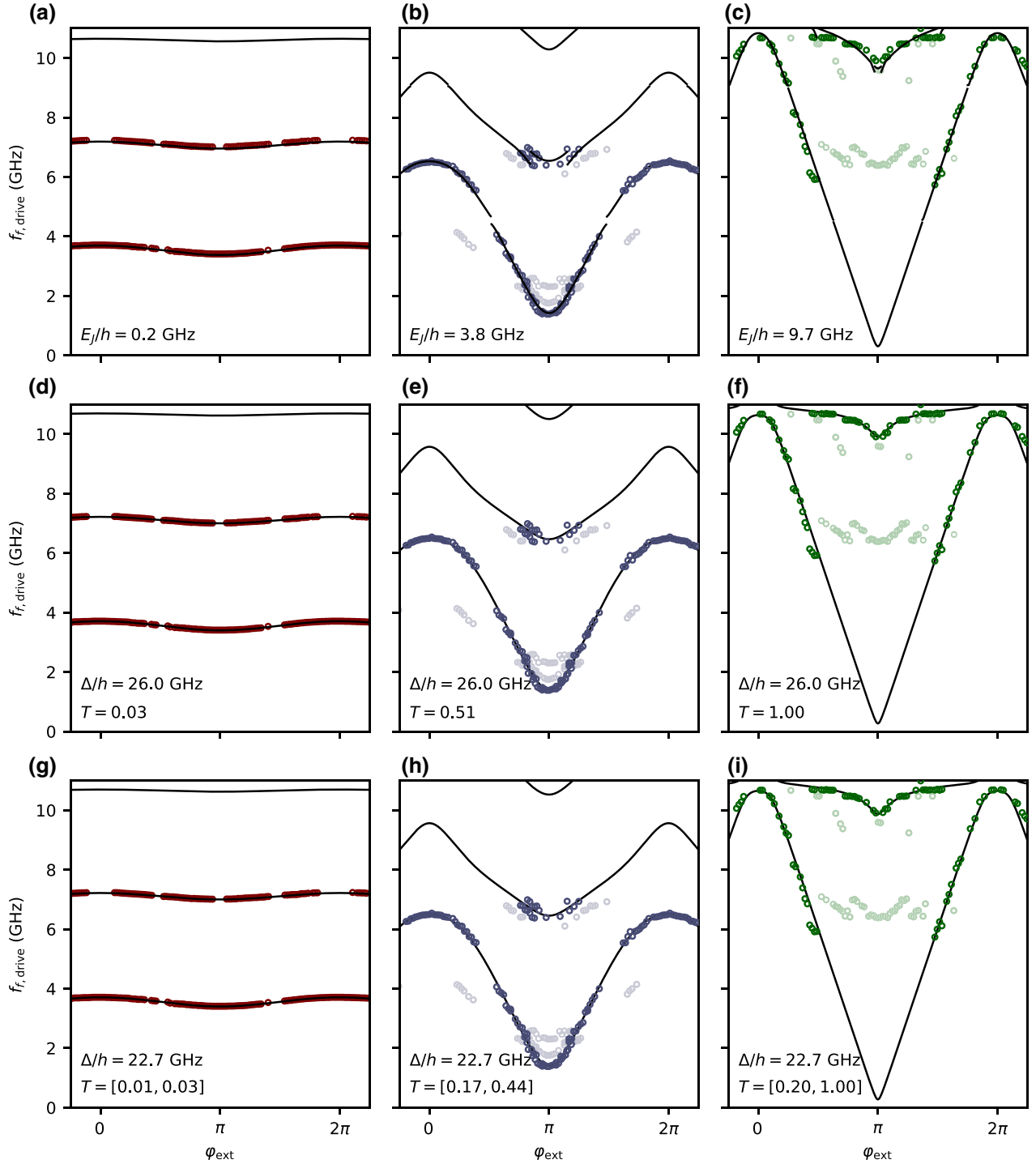
FIG. 6.   Fits using the Andreev potential in the Hamiltonian. Spectroscopy data fit with the uncoupled fluxonium Hamiltonian [Eq. (2)] with a sinusoidal potential (first row), with a one-channel potential (second row), and with a two-channel potential (third row). Only the dark markers, corresponding to transitions starting from the ground state, are included in the fit. We obtain $E_C/h = 2.35$ GHz and $E_L/h = 0.7$ GHz for the three different fits. The rest of the fit parameters are indicated in the different panels.

are considered. We thus cannot extract a measure of the number of junction channels by performing fits of the spectroscopic data.

    We furthermore observe that the best fit assuming a single channel occurs at $\Delta = 26$ GHz. This is smaller than the

gap ($\Delta = 53$ GHz) typically measured in transport experiments. This discrepancy may be due to the necessity of incorporating excited Andreev states into the fluxonium model or interactions due to an accidental quantum dot in the junction [42,56,57].
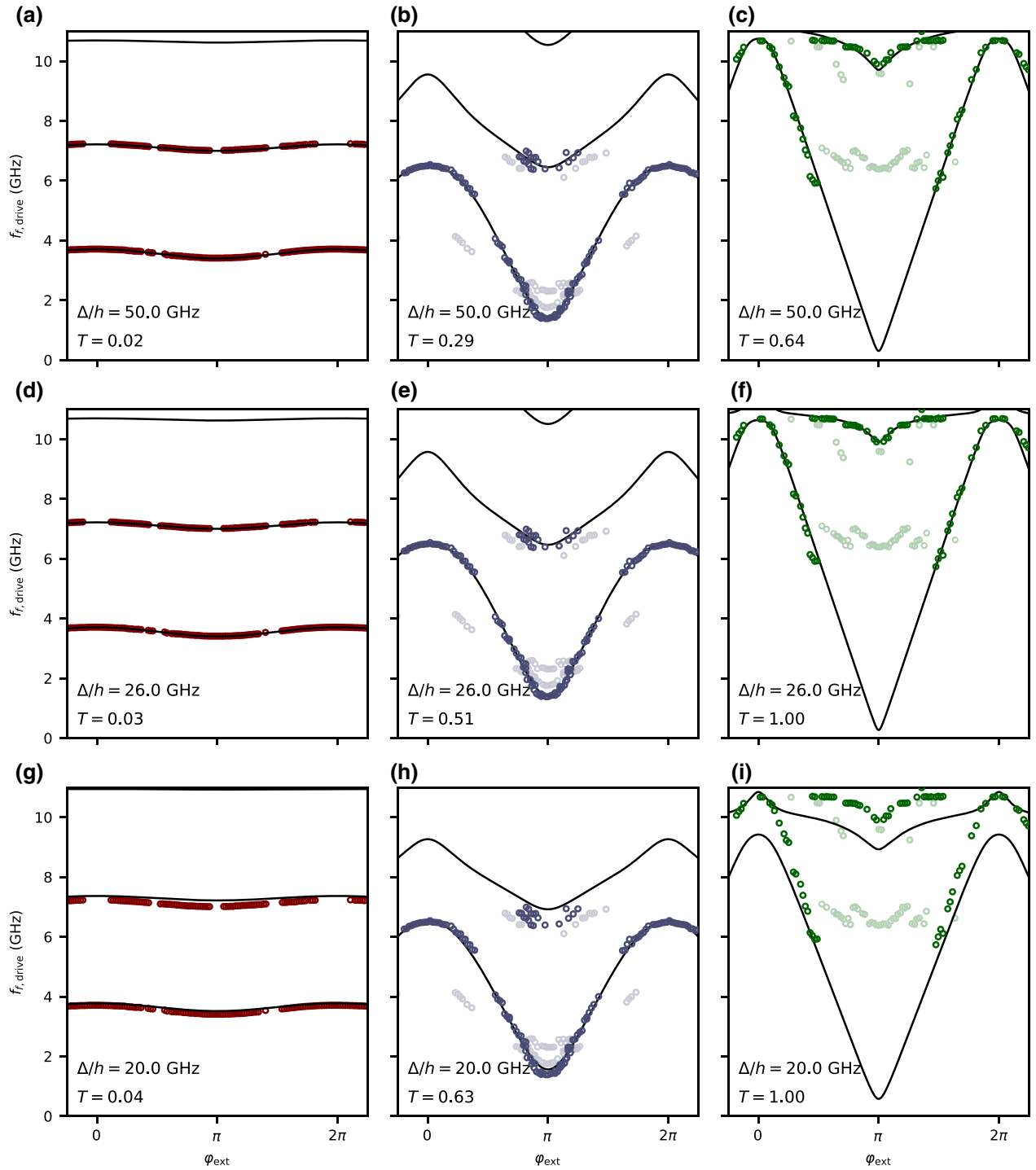
FIG. 7. The Δ dependence of fits using the Andreev potential in the Hamiltonian. Spectroscopy data fitted with the uncoupled fluxonium Hamiltonian [Eq. (2)] with a one-channel potential. In the first and third rows the value of Δ is fixed to $\Delta/h = 50.0$ GHz and $\Delta/h = 20.0$ GHz, respectively. In the second row Δ is left free and $\Delta/h = 26.0$ GHz is obtained as the optimum value. Only the dark markers, corresponding to transitions starting from the ground state are included in the fit.

[1] A. Blais, R.-S. Huang, A. Wallraff, S. M. Girvin, and R. J. Schoelkopf, Cavity quantum electrodynamics for super-conducting electrical circuits: An architecture for quantum computation, Phys. Rev. A **69**, 062320 (2004).

[2] I. Chiorescu, P. Bertet, K. Semba, Y. Nakamura, C. J. P. M. Harmans, and J. E. Mooij, Coherent dynamics of a flux qubit coupled to a harmonic oscillator, Nature **431**, 159 (2004).

[3] A. Wallraff, D. I. Schuster, A. Blais, L. Frunzio, R.-S. Huang, J. Majer, S. Kumar, S. M. Girvin, and

R. J. Schoelkopf, Strong coupling of a single photon to a superconducting qubit using circuit quantum electrodynamics, Nature **431,** 162 (2004).

[4] G. de Lange, B. van Heck, A. Bruno, D. J. van Woerkom, A. Geresdi, S. R. Plissard, E. P. A. M. Bakkers, A. R. Akhmerov, and L. DiCarlo, Realization of Microwave Quantum Circuits Using Hybrid Superconducting-Semiconducting Nanowire Josephson Elements, Phys. Rev. Lett. **115,** 127002 (2015).

[5] T. W. Larsen, K. D. Petersson, F. Kuemmeth, T. S. Jespersen, P. Krogstrup, J. Nygård, and C. M. Marcus, Semiconductor-Nanowire-Based Superconducting Qubit, Phys. Rev. Lett. **115,** 127001 (2015).

[6] F. Luthi, T. Stavenga, O. W. Enzing, A. Bruno, C. Dickel, N. K. Langford, M. A. Rol, T. S. Jespersen, J. Nygård, P. Krogstrup, and L. DiCarlo, Evolution of Nanowire Transmon Qubits and Their Coherence in a Magnetic Field, Phys. Rev. Lett. **120,** 100502 (2018).

[7] M. Hays, G. de Lange, K. Serniak, D. J. van Woerkom, D. Bouman, P. Krogstrup, J. Nygård, A. Geresdi, and M. H. Devoret, Direct Microwave Measurement of Andreev-Bound-State Dynamics in a Semiconductor-Nanowire Josephson Junction, Phys. Rev. Lett. **121,** 047001 (2018).

[8] X. Mi, J. V. Cady, D. M. Zajac, P. W. Deelman, and J. R. Petta, Strong coupling of a single electron in silicon to a microwave photon, Science **355,** 156 (2017).

[9] L. Casparis, M. R. Connolly, M. Kjaergaard, N. J. Pearson, A. Kringhøj, T. W. Larsen, F. Kuemmeth, T. Wang, C. Thomas, S. Gronin, G. C. Gardner, M. J. Manfra, C. M. Marcus, and K. D. Petersson, Superconducting gatemon qubit based on a proximitized two-dimensional electron gas, Nat. Nanotechnol. **13,** 915 (2018).

[10] J. G. Kroll, W. Uilhoorn, K. L. van der Enden, D. de Jong, K. Watanabe, T. Taniguchi, S. Goswami, M. C. Cassidy, and L. P. Kouwenhoven, Magnetic field compatible circuit quantum electrodynamics with graphene Josephson junctions, Nat. Commun. **9,** 4615 (2018).

[11] J. I.-J. Wang, D. Rodan-Legrain, L. Bretheau, D. L. Campbell, B. Kannan, D. Kim, M. Kjaergaard, P. Krantz, G. O. Samach, F. Yan, J. L. Yoder, K. Watanabe, T. Taniguchi, T. P. Orlando, S. Gustavsson, P. Jarillo-Herrero, and W. D. Oliver, Coherent control of a hybrid superconducting circuit made with graphene-based van der waals heterostructures, Nat. Nanotechnol. **14,** 120 (2019).

[12] M. Hays, V. Fatemi, K. Serniak, D. Bouman, S. Diamond, G. de Lange, P. Krogstrup, J. Nygård, A. Geresdi, and M. H. Devoret, Continuous monitoring of a trapped superconducting spin, Nat. Phys. **16,** 1103 (2020).

[13] A. Zazunov, A. Brunetti, A. L. Yeyati, and R. Egger, Quasiparticle trapping, Andreev level population dynamics, and charge imbalance in superconducting weak links, Phys. Rev. B **90,** 104508 (2014).

[14] J. I. Väyrynen, G. Rastelli, W. Belzig, and L. I. Glazman, Microwave signatures of Majorana states in a topological Josephson junction, Phys. Rev. B **92,** 134508 (2015).

[15] B. van Heck, J. I. Väyrynen, and L. I. Glazman, Zeeman and spin-orbit effects in the Andreev spectra of nanowire junctions, Phys. Rev. B **96,** 075404 (2017).

[16] K. Yavilberg, E. Ginossar, and E. Grosfeld, Differentiating majorana from andreev bound states in a superconducting circuit, Phys. Rev. B **100,** 241408 (2019).

[17] F. Hassler, A. R. Akhmerov, and C. W. J. Beenakker, The top-transmon: A hybrid superconducting qubit for parity-protected quantum computation, New J. Phys. **13,** 095004 (2011).

[18] T. Hyart, B. van Heck, I. C. Fulga, M. Burrello, A. R. Akhmerov, and C. W. J. Beenakker, Flux-controlled quantum computation with Majorana fermions, Phys. Rev. B **88,** 035121 (2013).

[19] E. Ginossar and E. Grosfeld, Microwave transitions as a signature of coherent parity mixing effects in the Majorana-transmon qubit, Nat. Commun. **5,** 4772 (2014).

[20] J. P. T. Stenger, M. Hatridge, S. M. Frolov, and D. Pekker, Braiding quantum circuit based on the 4π Josephson effect, Phys. Rev. B **99,** 035307 (2019).

[21] A. Y. Kitaev, Unpaired majorana fermions in quantum wires, Phys.-Uspekhi **44,** 131 (2001).

[22] R. M. Lutchyn, E. P. A. M. Bakkers, L. P. Kouwenhoven, P. Krogstrup, C. M. Marcus, and Y. Oreg, Majorana zero modes in superconductor-semiconductor heterostructures, Nat. Rev. Mater. **3,** 52 (2018).

[23] M. Sato and Y. Ando, Topological superconductors: A review, Rep. Prog. Phys. **80,** 076501 (2017).

[24] S. D. Sarma, M. Freedman, and C. Nayak, Majorana zero modes and topological quantum computation, Npj Quantum Inf. **1,** 15001 (2015).

[25] D. Pekker, C.-Y. Hou, V. E. Manucharyan, and E. Demler, Proposal for Coherent Coupling of Majorana Zero Modes and Superconducting Qubits Using the 4π Josephson Effect, Phys. Rev. Lett. **111,** 107007 (2013).

[26] J. Paajaste, M. Amado, S. Roddaro, F. S. Bergeret, D. Ercolani, L. Sorba, and F. Giazotto, Pb/inas nanowire josephson junction with high critical current and magnetic flux focusing, Nano Lett. **15,** 1803 (2015).

[27] K. Zuo, V. Mourik, D. B. Szombati, B. Nijholt, D. J. van Woerkom, A. Geresdi, J. Chen, V. P. Ostroukh, A. R. Akhmerov, S. R. Plissard, D. Car, E. P. A. M. Bakkers, D. I. Pikulin, L. P. Kouwenhoven, and S. M. Frolov, Supercurrent Interference in Few-Mode Nanowire Josephson Junctions, Phys. Rev. Lett. **119,** 187704 (2017).

[28] S. Hart, Z. Cui, G. Ménard, M. Deng, A. E. Antipov, R. M. Lutchyn, P. Krogstrup, C. M. Marcus, and K. A. Moler, Current-phase relations of inas nanowire josephson junctions: From interacting to multimode regimes, Phys. Rev. B **100,** 064523 (2019).

[29] D. J. van Woerkom, A. Proutski, B. van Heck, D. Bouman, J. I. Väyrynen, L. I. Glazman, P. Krogstrup, J. Nygård, L. P. Kouwenhoven, and A. Geresdi, Microwave spectroscopy of spinful Andreev bound states in ballistic semiconductor Josephson junctions, Nat. Phys. **13,** 876 (2017).

[30] L. Tosi, C. Metzger, M. F. Goffman, C. Urbina, H. Pothier, S. Park, A. L. Yeyati, J. Nygård, and P. Krogstrup, Spin-Orbit Splitting of Andreev States Revealed by Microwave Spectroscopy, Phys. Rev. X **9,** 011010 (2019).

[31] C. Janvier, L. Tosi, L. Bretheau, Ç. Ö. Girit, M. Stern, P. Bertet, P. Joyez, D. Vion, D. Esteve, M. F. Goffman, H. Pothier, and C. Urbina, Coherent manipulation of andreev states in superconducting atomic contacts, Science **349,** 1199 (2015).

[32] P. Krogstrup, N. L. B. Ziino, W. Chang, S. M. Albrecht, M. H. Madsen, E. Johnson, J. Nygård, C. M. Marcus, and

T. S. Jespersen, Epitaxy of semiconductor-superconductor nanowires, Nat. Mater. **14**, 400 (2015).

[33] V. E. Manucharyan, Ph.D. Thesis, School Yale University, 2012.

[34] V. E. Manucharyan, J. Koch, L. I. Glazman, and M. H. Devoret, Fluxonium: Single Cooper-pair circuit free of charge offsets, Science **326**, 113 (2009).

[35] K. Kalashnikov, W. T. Hsieh, W. Zhang, W.-S. Lu, P. Kamenov, A. Di Paolo, A. Blais, M. E. Gershenson, and M. Bell, Bifluxon: Fluxon-parity-protected superconducting qubit, PRX Quantum **1**, 010307 (2020).

[36] H. Rotzinger, S. T. Skacel, M. Pfirrmann, J. N. Voss, J. Münzberg, S. Probst, P. Bushev, M. P. Weides, A. V. Ustinov, and J. E. Mooij, Aluminium-oxide wires for superconducting high kinetic inductance circuits, Superconductor Sci. Technol. **30**, 025002 (2016).

[37] L. Grünhaupt, N. Maleeva, S. T. Skacel, M. Calvo, F. Levy-Bertrand, A. V. Ustinov, H. Rotzinger, A. Monfardini, G. Catelani, and I. M. Pop, Loss Mechanisms and Quasiparticle Dynamics in Superconducting Microwave Resonators Made of Thin-Film Granular Aluminum, Phys. Rev. Lett. **121**, 117001 (2018).

[38] N. Maleeva, L. Grünhaupt, T. Klein, F. Levy-Bertrand, O. Dupre, M. Calvo, F. Valenti, P. Winkel, F. Friedrich, W. Wernsdorfer, A. V. Ustinov, H. Rotzinger, A. Monfardini, M. V. Fistul, and I. M. Pop, Circuit quantum electrodynamics of granular aluminum resonators, Nat. Commun. **9**, 3889 (2018).

[39] L. Grünhaupt, M. Spiecker, D. Gusenkova, N. Maleeva, S. T. Skacel, I. Takmakov, F. Valenti, P. Winkel, H. Rotzinger, W. Wernsdorfer, A. V. Ustinov, and I. M. Pop, Granular aluminium as a superconducting material for high-impedance quantum circuits, Nat. Mater. **18**, 816 (2019).

[40] A. J. Annunziata, D. F. Santavicca, L. Frunzio, G. Catelani, M. J. Rooks, A. Frydman, and D. E. Prober, Tunable superconducting nanoinductors, Nanotechnology **21**, 445202 (2010).

[41] N. Samkharadze, A. Bruno, P. Scarlino, G. Zheng, D. P. DiVincenzo, L. DiCarlo, and L. M. K. Vandersypen, High-Kinetic-Inductance Superconducting Nanowire Resonators for Circuit QED in a Magnetic Field, Phys. Rev. Appl. **5**, 044004 (2016).

[42] T. M. Hazard, A. Gyenis, A. Di Paolo, A. T. Asfaw, S. A. Lyon, A. Blais, and A. A. Houck, Nanowire Superinductance Fluxonium Qubit, Phys. Rev. Lett. **122**, 010504 (2019).

[43] G. Stan, S. B. Field, and J. M. Martinis, Critical Field for Complete Vortex Expulsion from Narrow Superconducting Strips, Phys. Rev. Lett. **92**, 097003 (2004).

[44] O. V. Astafiev, L. B. Ioffe, S. Kafanov, Y. A. Pashkin, K. Y. Arutyunov, D. Shahar, O. Cohen, and J. S. Tsai, Coherent quantum phase slip, Nature **484**, 355 (2012).

[45] P. Winkel, K. Borisov, L. Grünhaupt, D. Rieger, M. Spiecker, F. Valenti, A. V. Ustinov, W. Wernsdorfer, and I. M. Pop, Implementation of a Transmon Qubit Using Superconducting Granular Aluminum, Phys. Rev. X **10**, 031032 (2020).

[46] W. C. Smith, A. Kou, U. Vool, I. M. Pop, L. Frunzio, R. J. Schoelkopf, and M. H. Devoret, Quantization of inductively shunted superconducting circuits, Phys. Rev. B **94**, 144507 (2016).

[47] See Supplemental Material at http://link.aps.org/supplemental/10.1103/PhysRevApplied.14.064038, which contains a theoretical description of the uncoupled fluxonium and additional field data for devices *A* and *B*.

[48] T. Yokoyama, M. Eto, and Y. V. Nazarov, Anomalous Josephson effect induced by spin-orbit interaction and Zeeman effect in semiconductor nanowires, Phys. Rev. B **89**, 195407 (2014).

[49] D. B. Szombati, S. Nadj-Perge, D. Car, S. R. Plissard, E. P. A. M. Bakkers, and L. P. Kouwenhoven, Josephson ϕ_0-junction in nanowire quantum dots, Nat. Phys. **12**, 568 (2016).

[50] Y. Huang, H. Pan, C.-X. Liu, J. D. Sau, T. D. Stanescu, and S. Das Sarma, Metamorphosis of andreev bound states into majorana bound states in pristine nanowires, Phys. Rev. B **98**, 144511 (2018).

[51] F. Dolcini, M. Houzet, and J. S. Meyer, Topological Josephson ϕ_0 junctions, Phys. Rev. B **92**, 035428 (2015).

[52] S. Wu, V. Fatemi, Q. D. Gibson, K. Watanabe, T. Taniguchi, R. J. Cava, and P. Jarillo-Herrero, Observation of the quantum spin hall effect up to 100 kelvin in a monolayer crystal, Science **359**, 76 (2018).

[53] Y. Cao, D. Rodan-Legrain, O. Rubies-Bigorda, J. M. Park, K. Watanabe, T. Taniguchi, and P. Jarillo-Herrero, Tunable correlated states and spin-polarized phases in twisted bilayer–bilayer graphene, Nature **583**, 215 (2020).

[54] X. Liu, Z. Hao, E. Khalaf, J. Y. Lee, Y. Ronen, H. Yoo, D. Haei Najafabadi, K. Watanabe, T. Taniguchi, A. Vishwanath, and P. Kim, Tunable spin-polarized correlated states in twisted double bilayer graphene, Nature **583**, 221 (2020).

[55] C. W. J. Beenakker, Universal Limit of Critical-Current Fluctuations in Mesoscopic Josephson Junctions, Phys. Rev. Lett. **67**, 3836 (1991).

[56] A. Bargerbos, W. Uilhoorn, C.-K. Yang, P. Krogstrup, L. P. Kouwenhoven, G. de Lange, B. van Heck, and A. Kou, Observation of Vanishing Charge Dispersion of a Nearly Open Superconducting Island, Phys. Rev. Lett. **124**, 246802 (2020).

[57] A. Kringhøj, B. van Heck, T. W. Larsen, O. Erlandsson, D. Sabonis, P. Krogstrup, L. Casparis, K. D. Petersson, and C. M. Marcus, Suppressed Charge Dispersion via Resonant Tunneling in a Single-Channel Transmon, Phys. Rev. Lett. **124**, 246803 (2020).